

1 **The Bacterial Cell Envelope as Delimiter of Anti-Infective Bioavailability – An *In Vitro***  
2 **Permeation Model of the Gram-Negative Bacterial Inner Membrane**

3  
4 Florian Graef<sup>a</sup>, Branko Vukosavljevic<sup>a</sup>, Jean-Philippe Michel<sup>b</sup>, Marius Wirth<sup>c</sup>, Oliver Ries<sup>c</sup>,  
5 Chiara De Rossi<sup>a</sup>, Maike Windbergs<sup>a</sup>, Véronique Rosilio<sup>b</sup>, Christian Ducho<sup>c</sup>, Sarah Gordon<sup>a\*</sup>  
6 and Claus-Michael Lehr<sup>a,d\*</sup>

7  
8  
9 <sup>a</sup> Helmholtz Institute for Pharmaceutical Research Saarland (HIPS), Helmholtz Center for  
10 Infection Research (HZI), Department of Drug Delivery, Campus E8 1, 66123 Saarbrücken,  
11 Germany

12 E-mail: Florian.Graef@helmholtz-hzi.de, Branko.Vukosavljevic@helmholtz-hzi.de, Maike.  
13 Windbergs@helmholtz-hzi.de, Chiara.DeRossi@helmholtz-hzi.de,  
14 Sarah.Gordon@helmholtz-hzi.de, Claus-Michael.Lehr@helmholtz-hzi.de

15 <sup>b</sup> Institut Galien Paris Sud, UMR 8612, Univ Paris-Sud, CNRS, Université Paris-Saclay, 5 rue  
16 J.B. Clément, F-92290 Châtenay-Malabry, France

17 E-Mail: jean-philippe.michel@u-psud.fr, veronique.rosilio@u-psud.fr

18 <sup>c</sup> Saarland University, Department of Pharmacy, Pharmaceutical and Medicinal Chemistry,  
19 Campus C2 3, 66123 Saarbrücken, Germany

20 E-Mail: marius.wirth@uni-saarland.de, christian.ducho@uni-saarland.de

21 <sup>d</sup> Saarland University, Department of Pharmacy, Biopharmacy and Pharmaceutical  
22 Technology, Campus E8 1, 66123 Saarbrücken, Germany

23 \* Corresponding authors

24

25 **Abstract**

26 Gram-negative bacteria possess a unique and complex cell envelope, composed of an inner  
27 and outer membrane separated by an intermediate cell wall-containing periplasm. This  
28 tripartite structure acts intrinsically as a significant biological barrier, often limiting the  
29 permeation of anti-infectives, and so preventing such drugs from reaching their target.  
30 Furthermore, identification of the specific permeation-limiting envelope component proves  
31 difficult in the case of many anti-infectives, due to the challenges associated with isolation of  
32 individual cell envelope structures in bacterial culture. The development of an *in vitro*  
33 permeation model of the Gram-negative inner membrane, prepared by repeated coating of  
34 physiologically-relevant phospholipids on Transwell<sup>®</sup> filter inserts, is therefore reported, as a  
35 first step in the development of an overall cell envelope model. Characterization and  
36 permeability investigations of model compounds as well as anti-infectives confirmed the

37 suitability of the model for quantitative and kinetically-resolved permeability assessment, and  
38 additionally confirmed the importance of employing bacteria-specific base materials for more  
39 accurate mimicking of the inner membrane lipid composition - both advantages compared to  
40 the majority of existing *in vitro* approaches. Additional incorporation of further elements of  
41 the Gram-negative bacterial cell envelope could ultimately facilitate model application as a  
42 screening tool in anti-infective drug discovery or formulation development.

43

44 Keywords: Gram-negative bacterial cell envelope, permeation kinetics, permeability  
45 investigations, *in vitro* permeation model

46

47	CL	cardiolipin
48	ER	electrical resistance
49	IM	inner membrane
50	KRB	Krebs-Ringer buffer
51	LC	liquid condensed
52	LE	liquid expanded
53	MIC	minimal inhibitory concentration
54	OM	outer membrane
55	PC	phosphatidylcholine
56	PL	phospholipid
57	$P_{app}$	apparent permeability coefficient
58	PBS	phosphate buffered saline
59	PMB	polymyxin B
60	POPE	1-hexadecanoyl-2-(9Z-octadecenoyl)- <i>sn</i> -glycero-3-phosphoethanolamine
61	POPG	1-hexadecanoyl-2-(9Z-octadecenoyl)- <i>sn</i> -glycero-3-phospho-(1'- <i>rac</i> -glycerol)

62	PVPA	phospholipid vesicle-based permeation assay
63	SE	standard error of the mean
64	SEM	scanning electron microscopy
65	UHPLC	ultra-high performance liquid chromatography

66

67

68

69

70

71

72

73

74

75

76

77

78

79

80

81

82

83

84

85

## 86 **1. Introduction**

87 The increasingly reported occurrence of multidrug-resistant bacteria, particularly those of the  
88 Gram-negative classification, constitutes a growing threat to the state of health worldwide  
89 [1,2]. The up-regulation and evolution of bacterial resistance mechanisms, leading to  
90 inadequate drug levels at target sites, in fact acts to exacerbate the already challenging task of  
91 successfully delivering anti-infective compounds or formulations into or across the cell  
92 envelope [3]. The unique and complex structure of the Gram-negative bacterial envelope  
93 operates intrinsically as a significant barrier, preventing the attainment of sufficient drug  
94 levels at required sites of action in many instances [4,5]. The envelope itself consists of an  
95 inner membrane (IM) of phosphatidylethanolamine, phosphatidylglycerol and cardiolipin as  
96 principal phospholipid (PL) components, together with an asymmetric outer membrane (OM)  
97 composed of a PL-containing inner leaflet and a lipopolysaccharide-containing outer leaflet.  
98 These two membrane structures, additionally incorporating aspects of active transport, are  
99 chiefly responsible for the intrinsic barrier properties of the envelope, which is therefore  
100 commonly termed as a two-membrane barrier [6]. In addition however, the periplasmic space  
101 separating the IM and OM serves as an area of high metabolic activity [7], and also houses the  
102 peptidoglycan cell wall (a much thinner structure in comparison to Gram-positive bacteria).  
103 The described intrinsic and resistance-compounded difficulties in achieving adequate drug  
104 levels at bacterial target sites, together with the present low flow within the antibiotic  
105 development pipeline, both contribute to a common inability to successfully treat Gram-  
106 negative bacterial infections. Such difficulties can ultimately and collectively be regarded as  
107 symptoms of a bacterial bioavailability problem [8], which is of vital importance to address.  
108 The development of new anti-infective compound classes, the discovery of new targets, and  
109 the advent of novel delivery strategies which facilitate effective anti-infective drug  
110 penetration into or completely across the cell envelope (in order to reach intracellular sites of

111 action) therefore all constitute important areas of research in this respect. In addition, research  
112 efforts within these areas require an increased understanding of and ability to investigate  
113 bacterial permeation processes - a difficult task to achieve currently *in cellulo* due to  
114 numerous associated challenges [8]. As such, a further research need to be addressed is the  
115 requirement for models which allow for the characterization and quantification of anti-  
116 infective permeation across the Gram-negative bacterial cell envelope. Such models would  
117 provide complementary information to that obtained from established, '*in cellulo*' efficacy  
118 testing approaches (such as determination of minimum inhibitory concentrations (MIC)),  
119 allowing for optimization of drug candidates with respect to their target interaction as well as  
120 their ability to sufficiently permeate the envelope barrier [9].

121  
122 A variety of *in vitro* models in fact already exist for investigating interactions between anti-  
123 infective compounds and bacterial cell envelope components; these can generally be classified  
124 as electrophysiology models [10,11], Langmuir films [12] and vesicle-based assays [13].  
125 While all such models are able to provide insight into bacterial permeation processes, they  
126 also demonstrate several shortcomings. For instance, most focus on approximating the IM or  
127 the OM alone, rather than both structures together (although some progress in this respect has  
128 been recently made [14]). Furthermore, the PL composition of existing IM models often  
129 deviates from that found in Gram-negative bacteria, in terms of either character or ratio [15].  
130 The majority of the available approaches also do not allow for the quantification of  
131 permeation processes [14, 16-18], an important ability which would allow for more in-depth  
132 and accurate characterization of the way in which anti-infective compounds and formulations  
133 interact with the bacterial envelope barrier [19]. Hence, there is a great need for new models  
134 which represent the entire Gram-negative bacterial envelope with respect to both composition  
135 and structure, and which are specifically designed to yield high content, quantitative  
136 permeation information in a kinetically- and ultimately spatially-resolved manner.

137

138 As a first step in the production of an overall envelope model, this work is aimed at designing  
139 and characterizing an *in vitro* model of the Gram-negative bacterial IM employing bacteria-  
140 specific PLs, which is explicitly designed to quantify the passive permeation kinetics of anti-  
141 infectives. A Transwell<sup>®</sup>-based setup, mimicking the conventional procedure to assess  
142 permeation through mammalian cell barriers, was employed for the model preparation  
143 process. An existing approach for production of lipid-based mammalian membrane models –  
144 the phospholipid-vesicle based permeation assay (PVPA) [20] - was adapted in order to  
145 prepare the bacterial IM model, utilizing a bacteria-specific lipid composition as found in the  
146 IM of Gram-negative bacteria such as *Escherichia coli* and *Pseudomonas aeruginosa* [21].  
147 The resulting preparation procedure was also employed to produce a model consisting solely  
148 of phosphatidylcholine, as a major phospholipid in mammalian cell membranes [20]. The IM  
149 model and the phosphatidylcholine-containing mammalian model (‘mammalian comparator’)  
150 were then directly compared at each stage of IM characterization and in subsequent  
151 permeability studies. This comparison was made in order to discern any lipid-dependent  
152 differences between the models in terms of structure and function, and in doing so, to clearly  
153 demonstrate the need to adapt an already existing mammalian lipid-based model using  
154 bacteria-relevant materials. Models were characterized with respect to the interfacial behavior  
155 of their component lipids, as well as integrity and robustness, topography, and thickness.  
156 Furthermore, sets of model compounds including anti-infectives were utilized to ultimately  
157 assess the impact of model lipid composition on permeability behavior, and to highlight the  
158 ability to obtain quantitative and kinetically-resolved permeation data.

159

## 160 **2. Material and methods**

161

### 162 *2.1. Materials*

163 1-hexadecanoyl-2-(9Z-octadecenoyl)-*sn*-glycero-3-phosphoethanolamine (POPE), 1-  
164 hexadecanoyl-2-(9Z-octadecenoyl)-*sn*-glycero-3-phospho-(1'-*rac*-glycerol) (sodium salt)  
165 (POPG) and 1,1',2,2'-tetra-(9Z-octadecenoyl) cardiolipin (sodium salt) (CL) purchased from  
166 Avanti Polar Lipids Inc. (Alabaster, AL, USA) were used for the IM model preparation. Egg  
167 phosphatidylcholine (PC, Lipoid E80) was kindly donated by Lipoid GmbH (Ludwigshafen,  
168 Germany), and employed for the mammalian comparator model. Polycarbonate filters with a  
169 pore size of 800 nm (Merck Millipore, Darmstadt, Germany) were used for liposome  
170 extrusion. Commercially available cell culture inserts (Transwell® permeable supports 3460)  
171 were obtained from Corning Inc. (Acton, MA, USA). Calcein, sodium fluorescein, rhodamine  
172 123, rhodamine B, rhodamine B isothiocyanate, atenolol, metoprolol tartrate, timolol maleate,  
173 nadolol, acebutolol hydrochloride and alprenolol hydrochloride (Sigma-Aldrich Co., St.  
174 Louis, MO, USA) served as model drugs. Polymyxin B (PMB), minocycline hydrochloride  
175 and ciprofloxacin hydrochloride (Sigma-Aldrich Co., St. Louis, MO, USA) were employed as  
176 anti-infective agents. All reagents for ultra-high performance liquid chromatography  
177 (UHPLC) were purchased from VWR (Radnor, PA, USA). All other chemicals and solvents  
178 were of at least analytical grade.

179

## 180 2.2 Methods

181

### 182 2.2.1 Langmuir trough experiments

183 Surface pressure-area  $\pi$ -A measurements of lipid monolayers composed of pure bacteria-  
184 relevant PLs (POPE, POPG, CL), their 70:20:10 weight mixture [21], or pure PC were  
185 performed using a thermostated Langmuir film trough (775.75 cm<sup>2</sup>, Biolin Scientific, Finland)  
186 enclosed in a plexiglas box. Experiments were performed at 294 and 303 K (21±1 °C and  
187 30±1 °C respectively). PLs were dissolved in a mixture of chloroform and methanol (9:1 v/v)  
188 to form solutions of 1 x 10<sup>15</sup> molecules/μl. These solutions were then used to spread PLs at

189 the air/buffer interface, following subphase cleaning by suction. After PL deposition, the  
190 system was left for 15 min to allow complete evaporation of the organic solvents. Monolayer  
191 compression was then performed at a speed of  $5 \text{ \AA}^2 \cdot \text{molecule}^{-1} \cdot \text{min}^{-1}$ . The results reported  
192 are mean values of at least two measurements. The surface compressional moduli (K) of  
193 monolayers were calculated from equation (1):

$$195 \quad K = -A \cdot \left( \frac{d\pi}{dA} \right) \quad (1)$$

196  
197 where A is the PL molecular area ( $\text{\AA}^2$ ),  $d\pi$  the surface pressure change (mN/m) and dA is the  
198 change in the molecular area.

### 200 *2.2.2 Model preparation*

201 Both the bacterial IM and the mammalian comparator model were produced by adapting the  
202 PVPA approach [20]. Liposomes composed of bacteria- or mammal-relevant PLs were first  
203 prepared via the lipid film hydration method [22]. Briefly, POPE, POPG and CL were used in  
204 a 70:20:10 weight ratio, as a bacteria-specific PL mixture. PC was used as mammal-specific  
205 PL. POPE, POPG and CL, or PC alone were dissolved in a mixture of chloroform and  
206 methanol (3:1, 5 ml) in a round-bottom flask (250 ml). Organic solvents were then removed  
207 under reduced pressure (1 h: 200 mbar, 30 min: 40 mbar; 70 °C (bacteria-specific PL  
208 mixture); 55 °C (mammal-specific PL)) using a Rotavapor R-205 (BÜCHI Labortechnik  
209 GmbH, Essen, Germany) in order to form a thin lipid film. Phosphate buffered saline (PBS;  
210 adjusted to pH 7.4) containing ethanol (10% v/v) was used to rehydrate the lipid film to obtain  
211 the liposome dispersions (6% w/v total lipids). Afterwards, liposomes were sonicated for 1 h  
212 and subsequently extruded (10 times; at 70 °C in case of the bacteria-relevant liposomes and  
213 55 °C in case of the mammal-relevant liposomes), using a Liposofast L-50 extruder (Avestin



214 Europe GmbH, Mannheim, Germany). Both IM and mammalian comparator models were  
215 then prepared by three consecutive cycles of liposome addition (75  $\mu$ l each) onto filter  
216 supports, followed by centrifugation (30 min, 1040 g; Hettich Rotina 420 R, Hettich GmbH,  
217 Tuttlingen, Germany) and oven-drying (50 min, 50 °C), with a final freeze-thaw step (-80 °C,  
218 20 min; 45 °C for 20 min).

219

### 220 *2.2.3 Liposome size and surface charge measurements*

221 The hydrodynamic diameter and size distribution of liposomes was measured in PBS  
222 (adjusted to pH 7.4) using dynamic light scattering, while surface charge ( $\zeta$ -potential) was  
223 determined (in the same medium) using laser doppler micro-electrophoresis (Zetasizer Nano  
224 ZS, Malvern Instruments, UK).

225

### 226 *2.2.4 Confocal Raman microscopy*

227 Confocal Raman microscopy analysis was carried out to investigate the integrity of IM and  
228 mammalian comparator model lipid coatings using a WITec alpha 300R+ imaging system  
229 (WITec GmbH, Ulm, Germany), with an Olympus 50 x objective (N.A. 0.35). The excitation  
230 source was a diode laser with a wavelength of 785 nm (50 mW). Models were analyzed  
231 following preparation, and after 5 h incubation in Krebs-Ringer buffer (KRB) at 37 °C  
232 without any further sample alteration. A confocal pinhole of 100  $\mu$ m rejected signals from  
233 out-of-focus regions. Raman spectra were acquired every 100  $\mu$ m along the x- and y-axis  
234 across the entire model membrane area, with an integration time of 4 s. Cosmic ray removal  
235 and background subtraction were applied to all spectra, which were then processed using  
236 hierarchical cluster analysis and basis analysis as multivariate methods for data processing,  
237 and converted into spatially-resolved false-color images using WITec Project Plus software  
238 (WITec GmbH, Ulm, Germany).

239

240 *2.2.5. Laser scanning interferometry*

241 Model topography was analyzed via a LEXT OLS4000 3D Laser Measuring Microscope  
242 (Olympus AG, Tokyo, Japan), using a 405 nm semiconductor laser and a 20 x objective lens.  
243 Transwell® membranes with PL coatings were cut out of the plastic Transwell® holder  
244 surround and fixed on sample holders. Five representative membrane areas with an image size  
245 of approximately 5.6 mm<sup>2</sup> each were analyzed. The center of the overall model surface was  
246 denoted as area 1. The center of further imaged edge areas was set at a distance of 3000 µm  
247 from the upper (2), right (3), bottom (4) and left (5) margin of the overall membrane surface.

248

249 *2.2.6 Scanning electron microscopy*

250 For scanning electron microscopy (SEM) investigations, freshly prepared model membranes  
251 were first freeze-dried (Christ alpha 2-4 plus, Martin Christ Gefriertrocknungsanlagen GmbH,  
252 Osterode am Harz, Germany). As for laser scanning interferometry, Transwell® membranes  
253 with PL coatings were then cut out of the plastic holder surround; filter membranes were  
254 subsequently removed. Vertical cross-sections of model membranes prepared using a scalpel  
255 were then sputtered with gold, placed in a vertical manner on sample grids and subsequently  
256 analyzed via SEM (Zeiss EVO HD 15, Carl Zeiss AG, Oberkochen, Germany).

257

258 *2.2.7. Permeability investigations*

259 For investigation of permeability behavior, transport studies were performed with at least 6  
260 repetitions from 2 individual experiments. IM and mammalian comparator model-permeated  
261 amounts of fluorescent dyes and β-blockers were determined, as model compounds. Amounts  
262 of permeated ciprofloxacin and minocycline (with and without 1 h of model pre-incubation  
263 with 15.4 µM PMB), as well as an AlexaFluor® 488-labeled functionalized fatty acid moiety  
264 of the muraymycin A series of nucleoside antibiotics, together with corresponding reference

265 compound (both synthesized in-house according to Ries *et al.* [23]), were determined as anti-  
266 infective substances.

267

268 Prepared model membranes on Transwell® filter inserts were placed in cell culture plates and  
269 pre-incubated to rehydrate and equilibrate the system with pre-warmed KRB (pH 7.4, 37 °C)  
270 for 30 min (upon which electrical resistance (ER) values were seen to stabilize, see  
271 Supplementary Material). Following KRB removal, 520 µl of drug solution in KRB, in each  
272 case at a concentration calculated in order to ensure sink conditions and adjusted to pH 7.4  
273 (see Supplementary Material Tables S1 and S2, 1.27 µM in case of the functionalized fatty  
274 acid moiety and reference compound) was added to the apical compartment of each culture  
275 plate well (donor). A 1.5 ml volume of pre-warmed KRB was also added to the basolateral  
276 compartment (acceptor). A 20 µl volume of drug solution in KRB was immediately removed  
277 from the apical compartment, and employed to accurately measure the starting donor  
278 concentration. Samples of 200 µl were taken from the basolateral compartment of culture  
279 plate wells after 0, 0.5, 1, 1.5, 2, 2.5, 3.5 and 4.5 h, and used to quantify the permeated  
280 amount of applied compounds (see below). The removed volume was replaced with an equal  
281 volume of pre-warmed KRB in order to maintain sink conditions. Cell culture plates  
282 containing coated Transwell® filter inserts were placed on an orbital shaker (IKA®-Werke  
283 GmbH and Co KG, Staufen, Germany) set at 150 rpm and kept at 37 °C in an incubator for  
284 the duration of transport studies.

285

#### 286 *2.2.8. Quantification of permeated compound/drug amount and permeability calculations*

287 A Tecan Infinite® M200 plate reader (Tecan GmbH, Crailsheim, Germany) was used to  
288 determine the permeated amount of fluorescent dyes (see Supplementary Material Table S1).

289 A Dionex Ultimate® 3000 UHPLC with an Accucore column (RP 18, 150 mm x 2.1 mm, 2.6  
290 µm, Thermo Fisher Scientific Co., Waltham, MA, USA) was used to quantify the permeated

291 amount of  $\beta$ -blockers, ciprofloxacin and minocycline in transport studies.  $\beta$ -blocker  
292 quantification was carried out using a binary solvent system (A = 36.6 mM Na<sub>2</sub>HPO<sub>4</sub> + 33.4  
293 mM triethylamine adjusted to pH 3; B = acetonitrile) as eluent in different ratios, depending  
294 on the analyte; the flow rate and resulting compound retention time also varied (see  
295 Supplementary Material Table S2). The column oven temperature in all cases was set to 40  
296 °C. Ciprofloxacin and minocycline quantification was also carried out using a binary solvent  
297 system (A= 0.02 M Na<sub>2</sub>HPO<sub>4</sub> adjusted to pH 2.7; B= acetonitrile) as eluent in different ratios.  
298 The resulting retention time also varied (see Supplementary Material Table S2). The column  
299 oven temperature was set to 25 °C for ciprofloxacin and to 40 °C for minocycline. Permeated  
300 amounts of AlexaFluor<sup>®</sup> 488-labeled fatty acid moiety and corresponding reference  
301 compound were determined as described above for fluorescent dyes, with  $\lambda_{exc.}$  (nm) = 470 and  
302  $\lambda_{em.}$  (nm) = 520.

303

304 In all cases, the permeated compound amount was calculated in reference to calibration  
305 curves created from samples of standard concentration. The cumulative permeated compound  
306 amount was then plotted as a function of time. The slope of the linear region of this curve  
307 constitutes the rate of compound flux, which was used to calculate the apparent permeability  
308 coefficient ( $P_{app}$ ) of each compound according to equation (2):

$$309 \quad P_{app} \text{ (cm/sec)} = J/(A*c_0) \quad (2)$$

310

311 where J is the substance flux (mg/sec), A the surface area of the Transwell<sup>®</sup> filter insert (cm<sup>2</sup>)  
312 and  $c_0$  the initial compound concentration (mg/ml).

313

#### 314 2.2.9. Statistical analysis:

315 Where appropriate, presented numerical data represent mean  $\pm$  standard error of the mean  
316 (SE). Student's t-test was employed where relevant to evaluate significant differences ( $*=P <$

317 0.05, \*\*\*= $P < 0.001$ ). All tests were calculated using the software SigmaPlot version 12.5  
318 (Systat Software, Inc., San Jose, California, USA).

319

### 320 **3. Results and discussion**

321

322 *3.1. Bacterial IM and mammalian comparator membrane model preparation,*  
323 *characterization and comparison*

324

325 *3.1.1. Interfacial behavior comparison of bacteria- and mammal-relevant phospholipids*

326 Prior to IM model development and optimization the interfacial behavior of individual  
327 bacterial PLs, a bacterial PL mixture, and the mammal-specific PC was characterized using  
328 the Langmuir trough technique. Surface pressure-area measurements of pure POPE, POPG  
329 and CL monolayers were carried out, as well as the ternary mixture of POPE:POPG:CL in a  
330 relevant 70:20:10 weight ratio were carried out to confirm miscibility of the bacterial PL  
331 components. Investigation of PC lipid monolayers was also carried out in order to investigate  
332 the occurrence of any notable differences in behavior of PC and the bacterial PL mixture at  
333 the molecular level. Surface pressure-area isotherms were initially obtained at 21 °C, followed  
334 by the more physiologically relevant temperature of 30 °C (representing the highest  
335 temperature that could be applied in the experimental setup without the introduction of  
336 inaccuracies caused by buffer evaporation) (Fig. 1A). Isotherms were then used to calculate  
337 the compressibility moduli of PL monolayers (Fig. 1B).

338

339

340

341

342  
343  
344  
345  
346  
347  
348  
349  
350  
351  
352  
353  
354  
355  
356  
357  
358  
359  
360  
361  
362  
363  
364  
365  
366  
367

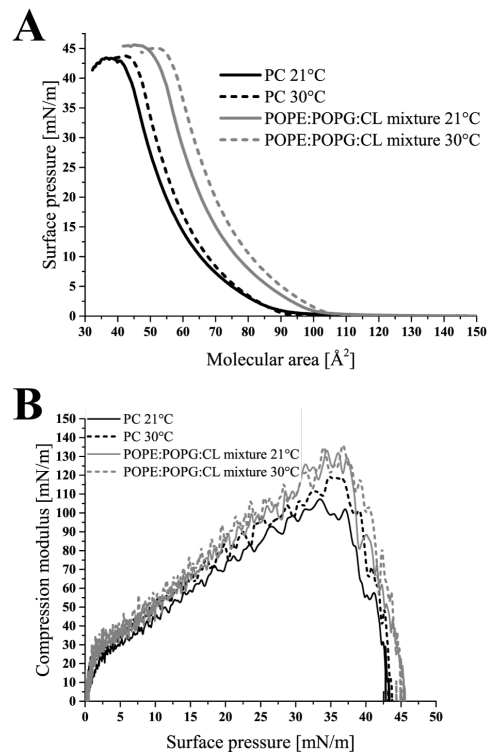


**Fig. 1.** Langmuir studies of bacterial IM and mammal-relevant PLs. Compression isotherms for bacteria-specific PL mixture (POPE:POPG:CL) and pure PC monolayers at 21 °C and 30 °C (A), showing differences in two-dimensional organization. Corresponding compressibility moduli as a function of surface pressure for both tested monolayers are additionally depicted (B), demonstrating the greater rigidity of the POPE:POPG:CL monolayer as compared to PC.

The isotherms obtained for the ternary bacterial PL mixture at 21 °C appeared to be intermediate between those of pure POPG and POPE (see Supplementary Material Fig. S1A), demonstrating that, although POPE is the major component of the ternary bacterial PL mixture, it is not the only mixture component contributing to the interfacial behavior. The influence of POPG and CL on the surface area-pressure measurements of POPE:POPG:CL monolayers, together with free energy of mixing and excess molecular area calculations (see Supplementary Material Fig. S1B, S1C) therefore implies the existence of a true lipid mixture. Comparison of the isotherms for the ternary mixture and pure PC monolayers revealed similar collapse pressures ( $\pi_c$ ) at both 21 °C and 30 °C (Fig. 1A), with values around

368 44 mN/m (Table 1). However, the isotherm-derived larger molecular areas for the lipid  
 369 mixture at pressure onset ( $A_{\text{onset}}$ ) and collapse ( $A_c$ ) account for more expanded monolayers of  
 370 the ternary mixture compared to those of pure PC.

371  
 372 **Table 1.** Summary of conducted Langmuir studies. Characteristic parameters of compression  
 373 isotherms, comparing the bacteria-relevant POPE:POPG:CL mixture to PC at 21 °C and 30  
 374 °C.

Applied		$A_{\text{onset}}$	$A_c$	$\pi_c$
Temperature (°C)	Monolayer	(Å <sup>2</sup> )	(Å <sup>2</sup> )	(mN/m)
21	POPE:POPG:CL	103.0	51.6	45.4
21	PC	97.5	43.5	42.9
30	POPE:POPG:CL	107.5	55.8	44.9
30	PC	92.3	45.4	43.5

382  
 383  $A_{\text{onset}}$ : molecular area at pressure onset,  $A_c$ : molecular area at collapse,  $\pi_c$ : surface pressure at  
 384 collapse

385  
 386 In addition to information gained directly from the isotherms, compressibility moduli were  
 387 calculated in order to determine the physical state of the PC and PL mixture monolayers at  
 388 various surface pressures. Compressibility moduli below 12.5 mN/m, in the range of 13-100  
 389 mN/m, from 100 to 250 mN/m and above 250 mN/m infer a gaseous, liquid expanded (LE),  
 390 liquid condensed (LC) and solid state of monolayers [24], respectively. PL organization at  
 391 surface pressures in the range of 25-35 mN/m is of particular interest, as this represents the  
 392 pressure range considered to correspond to the internal lateral pressure found in natural  
 393 membranes [25]. PC monolayers were found to be in an LE state at 21 °C within this surface

394 pressure range, whereas POPE:POPG:CL monolayers appeared to be in the LC state. PC  
395 monolayers were only observed to be in the LC state at higher surface pressures, from 30-38  
396 mN/m (Fig. 1B). A similar observation was made from measurements performed at 30 °C. As  
397 a result of this interfacial analysis, the bacterial PL mixture monolayer can be regarded as  
398 being greater in molecular area and slightly more rigid compared to that of PC, at both  
399 investigated temperatures; a first indication of differences in the behavior of bacteria- and  
400 mammal-specific lipids on a molecular level can therefore be inferred.

401

### 402 *3.1.2. Bacterial IM and mammalian membrane model preparation*

403 Following initial Langmuir studies, membrane models consisting of the previously employed  
404 POPE:POPG:CL in a 70:20:10 weight ratio (bacterial IM model) and pure PC (mammalian  
405 comparator model) were prepared, via the PVPA approach [20]. In this two-step approach,  
406 liposomes consisting of the PLs of interest are first prepared, as a means to facilitate lipid  
407 deposition onto Transwell® filter supports without the use of organic solvents; liposomes are  
408 then repeatedly coated onto filter supports in order to form a lipid membrane structure.  
409 Although serving only as a means for lipid deposition, prepared POPE:POPG:CL and PC  
410 liposomes were analyzed in terms of their hydrodynamic diameter and surface charge ( $\zeta$ -  
411 potential) in order to confirm a consistent outcome of liposome production. Low variation in  
412 z-average and surface charge of both POPE:POPG:CL and PC liposomes confirmed the  
413 acceptability of liposome preparation (see Supplementary Material Table S3), whereas  
414 differences between bacterial and mammalian lipid liposomes (for instance with respect to  
415 size) could be regarded as an outcome of the previous elucidated differences in PL packing  
416 properties (see section 3.1.1).

417

418 While PVPA models consisting of PC alone have been previously established [26-28], the  
419 primary objective of the current work was to develop a bacterial IM model. For this reason,

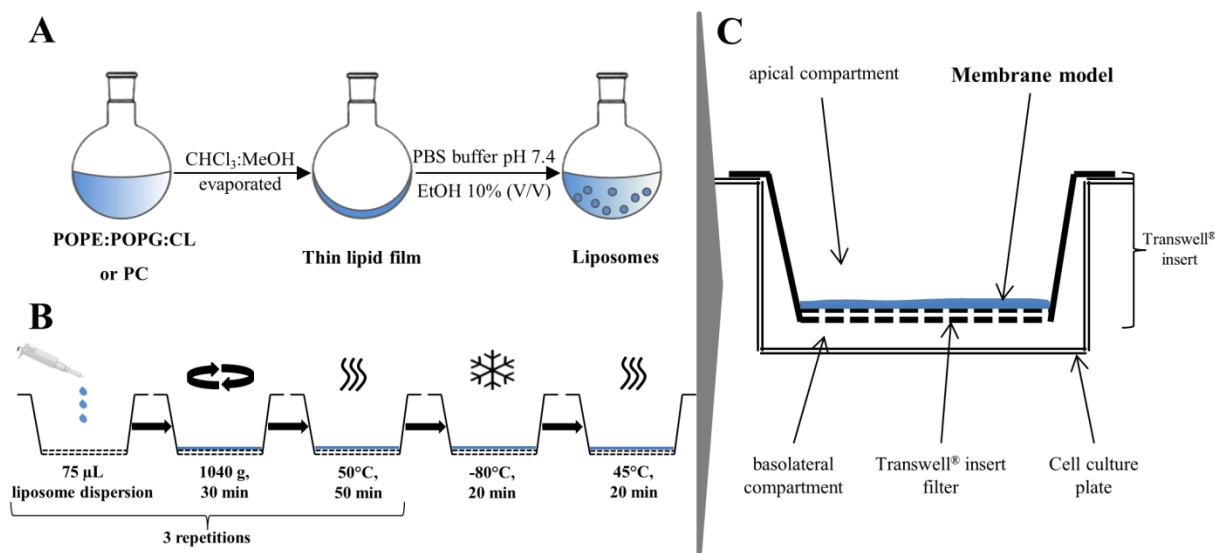


420 model preparation was adapted and optimized with respect to the use of POPE:POPG:CL.  
421 The IM-optimized preparation procedure was then applied using PC liposomes in order to  
422 produce a mammalian model which was truly comparative in nature. The procedure applied to  
423 deposit and coat liposomes on a Transwell® filter was required to result in the construction of  
424 an IM surrogate exhibiting robust permeation barrier properties, as well as a high level of  
425 stability on exposure to buffer (as would occur during transport studies). Thus, the model  
426 preparation procedure was optimized to fulfil these requirements. Deposition and coating  
427 parameters were refined by tracking the impact of parameter alterations on model barrier  
428 function in simulated transport experiments (entailing exposure to KRB, pH 7.4, 37 °C, for 5  
429 h). Barrier properties of the IM model were inferred from measurement of ER, a common  
430 means of monitoring barrier integrity in both cell-based [29,30] as well as cell-free [20]  
431 permeation models (See Supplementary Material Figure S2).

432  
433 The optimized preparation procedure (Fig. 2) consisted of three consecutive cycles of  
434 liposome addition to a Transwell® filter insert, centrifugation and drying, followed by a final  
435 freeze-thaw step – this step has been shown to promote liposome fusion, leading to a  
436 confluent PL coating (rather than layers of discrete liposomes) with stable barrier function  
437 [26]. The bacterial IM model constructed via this procedure showed sufficiently high and  
438 constant ER values throughout a 5 h period of exposure to KRB (see Supplementary Material  
439 Fig. S2), with no visible detachment of lipid coating from the Transwell® filter support. The  
440 described preparation procedure as optimized for IM model preparation was then used for  
441 preparation of a mammalian comparator model, by coating with PC liposomes. The  
442 comparator model also demonstrated a high and stable level of ER upon incubation with KRB  
443 (data not shown), as well as a lack of visible detachment from the Transwell® filter support.

444

445



446 **Fig. 2.** Model preparation procedure. Schematic of the two-step PVPA model preparation  
 447 procedure, consisting of liposome preparation (A) and subsequent coating with liposome  
 448 dispersions to form IM and mammalian comparator models (B). Liposomes consisting of  
 449 POPE, POPG and CL were used to construct the bacterial IM model, while PC liposomes  
 450 were employed to prepare the mammalian comparator. The final set-up of a model (blue)  
 451 placed on top of a Transwell® filter support is additionally shown (C).

452

### 453 3.1.3. Model integrity and topography assessment

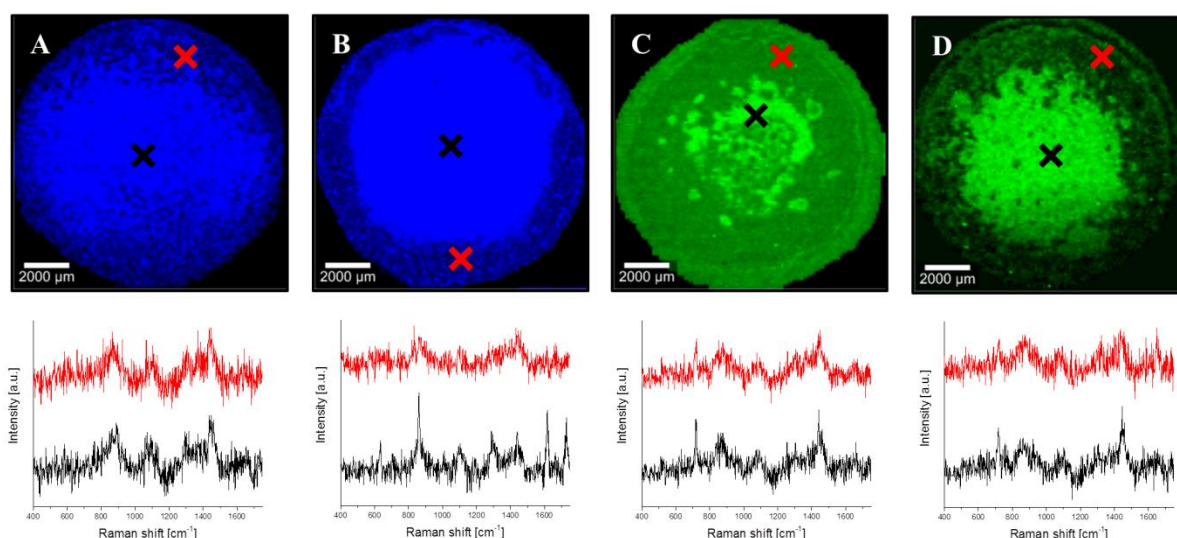
454 As described above, the optimized preparation procedure was seen in both the case of the IM  
 455 and mammalian comparator model to result in a stable and robust membrane structure with  
 456 appreciable barrier function. These properties can themselves be taken as an indication of a  
 457 continuous and uninterrupted coating of bacteria- or mammal-specific lipids on Transwell®  
 458 filter inserts. However, as any discontinuity present initially in the membrane structure or  
 459 developing during transport experiments has the potential to lead to overestimation of the  
 460 permeated amount of tested compounds/drugs and so distortion of resulting permeability data,  
 461 it was deemed necessary to further investigate and firmly establish model integrity.  
 462 Chemically selective analysis of the entire surface area of Transwell® filter inserts  
 463 accommodating either the IM or mammalian comparator model was therefore performed

464 using confocal Raman microscopy, to determine model integrity following preparation as well  
465 as following incubation in buffer (as described above for simulated transport studies). Due to  
466 the structured surface of the models, optical topography was applied prior to confocal Raman  
467 microscopy experiments in order to adjust the focus according to the sample topography, and  
468 to characterize topography of the overall model area. Topography profiles indicated a higher  
469 surface height at the edges compared to the center in the case of both models (see Supporting  
470 Information Figure S3). This was expected due to the model preparation procedure, and is in  
471 agreement with previous investigations [31].

472

473 Confocal Raman microscopy as such allows for label-free discrimination between the  
474 polyester material of the Transwell<sup>®</sup> filter inserts and the PLs of the membrane models, based  
475 on the individual spectra of the compounds. Consequently, the method allows for  
476 determination of the extent to which Transwell<sup>®</sup> filter inserts are covered with model PLs.  
477 Recorded Raman spectra were processed and subsequently converted into spatially-resolved  
478 false color images, in order to enable visualization of the integrity of lipid coating (Fig. 3,  
479 bacteria-relevant lipids of the IM model in blue, mammal-relevant lipids of the comparator  
480 model in green). Continuous bacterial PL coverage of Transwell<sup>®</sup> filter inserts was observed  
481 directly after IM model preparation, with no sign of coating defects (Fig. 3A); this continuous  
482 lipid coating was seen to remain entirely intact following 5 h incubation of the IM model in  
483 transport buffer (Fig. 3B). Likewise, the mammalian comparator model showed a continuous  
484 coverage and the absence of any defects in the PL layer immediately following preparation  
485 (Fig. 3C). Furthermore, no lipid-free Transwell<sup>®</sup> areas were observed following simulated  
486 transport experiments (Fig. 3D). Even though variations in Raman signal intensity translating  
487 to color intensity gradients could be observed in some images (especially Fig. 3D), overall  
488 intact PL coverage was confirmed by the presence of lipid-specific peaks over the entire  
489 Transwell<sup>®</sup> filter area in both models, before and after exposure to KRB. For illustration, the

490 individual raw Raman spectra derived from the central as well as from the outer region of  
491 coated filter membranes (marked by black and red crosses respectively) are presented below  
492 each of the Raman images in Fig. 3. The confirmed integrity of both the bacterial IM and  
493 mammalian comparator models, together with the earlier demonstrated appropriate and stable  
494 model barrier properties, therefore indicates the feasibility of compound permeability  
495 determination in the IM and comparison with the mammalian comparator.



496 **Fig. 3.** Integrity assessment of the IM and mammalian comparator model. False color images  
497 with representative single Raman spectra of central and outer regions of coated Transwell®  
498 filter inserts, showing the IM model with bacteria-relevant lipids indicated in blue before (A)  
499 and after (B) exposure to KRB, as well as mammal-relevant lipids of the comparator model in  
500 green before (C) and after (D) exposure to buffer. The presence of lipid-specific Raman peaks  
501 in all single Raman spectra at  $1440\text{ cm}^{-1}$  (in raw state without any further spectral  
502 manipulation, e.g. smoothing or subtraction) confirmed the overall lipid coverage. Color  
503 intensity differences represent the variation in Raman signal intensity, not a lesser degree of  
504 lipid coverage.

505

506 Having established that both the bacterial IM and mammalian comparator model were  
507 suitable for permeability investigations, the focus of further characterization shifted towards

508 comparison and contrast of model properties. Following initial optical topography  
509 investigations, laser scanning interferometry was employed to obtain more detailed insights  
510 into the topographical profiles of both the IM and mammalian comparator model following  
511 preparation. Hence, the bacterial IM model surface was analyzed at five representative  
512 positions (center; upper, right, bottom and left edges) each with an approximate image size of  
513 5.6 mm<sup>2</sup>, representing the maximum image size of the employed objective (Fig. 4A). A lower  
514 height maximum of approximately 73 μm, as well as a more uniform surface profile were  
515 found at the center of the IM model (Fig. 4B 1) as compared to the edge areas, which showed  
516 height maximums of up to 184 μm (Fig. 4B 2-5). The mammalian comparator model  
517 exhibited a similar contrast in surface height maximums and profile uniformity when  
518 comparing center and edge areas (Fig. 4C 1-5), indicating no marked differences in initial  
519 topography of IM and mammalian comparator models.

520

521

522

523

524

525

526

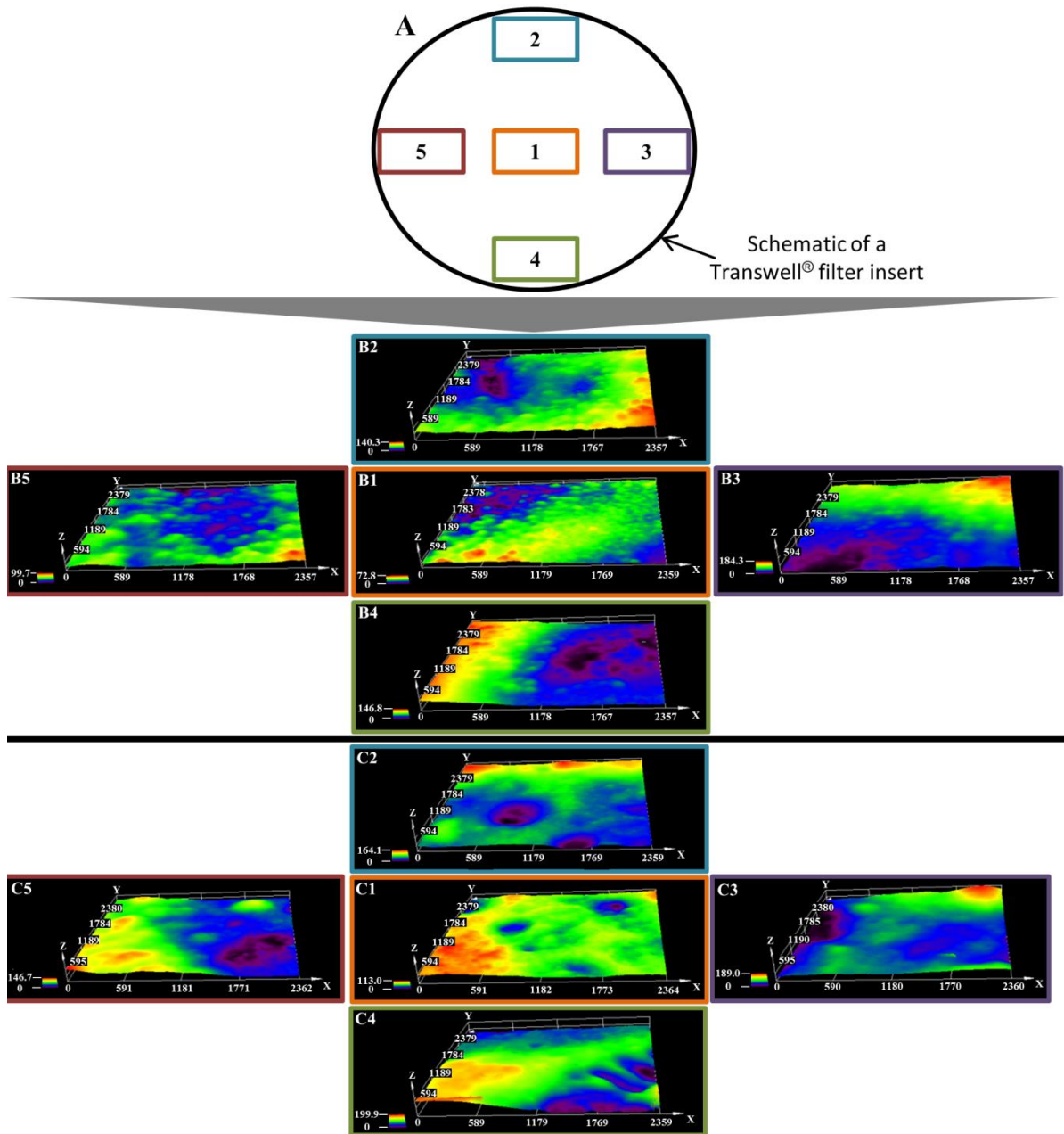
527

528

529

530

531



532 **Fig. 4.** Surface topography assessment of the IM and mammalian comparator model.  
 533 Schematic of the model surface showing the location of the representative imaged areas (A).  
 534 Topography of the bacterial IM model imaged at the five representative model areas (center  
 535 (B1), as well as upper (B2), right (B3), bottom (B4) and left (B5) edges) is shown. The same  
 536 areas of the mammalian comparator model (center (C1), upper (C2), right (C3), bottom (C4)  
 537 and left (C5) edges) were additionally imaged.

538

539

540

541 3.1.4. Model thickness assessment

542 Model thickness constitutes another parameter which potentially affects the permeability  
543 behavior of tested compounds/drugs [32]. Therefore, further to confirming model integrity  
544 and an absence of drastic differences in surface topography, it had to be ensured that the IM  
545 and the mammalian comparator model exhibited comparable values in the z dimension.  
546 Freeze-dried, vertical cross-sections of both models were therefore applied in their original  
547 orientation on sample grids and subsequently imaged and sized using SEM. Analysis of SEM  
548 images revealed similar thicknesses of the IM and the mammalian comparator model, with  
549 values of approximately 160  $\mu\text{m}$  in both cases (Fig. 5). SEM images additionally indicated  
550 differences in inner model morphology, potentially occurring as a result of the differences in  
551 employed PLs; this indication was further confirmed by cryo-SEM analysis of IM and  
552 mammalian comparator models (see Supplementary Material Figure S4).

553

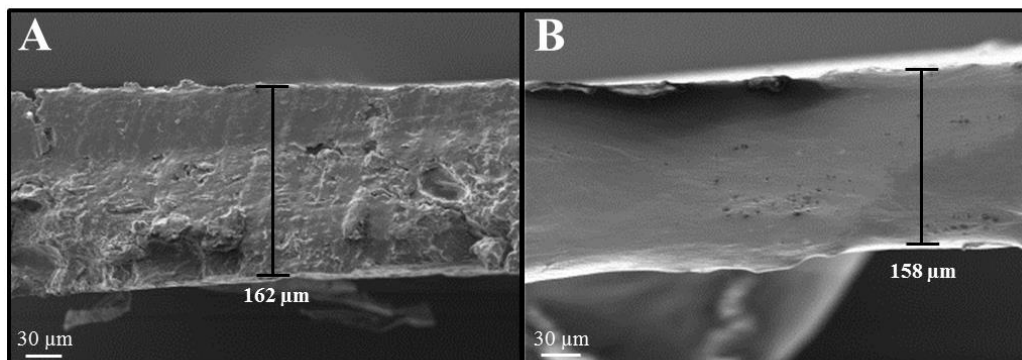
554

555

556

557

558



559 **Fig. 5.** Thickness evaluation of the IM and mammalian comparator model. Representative  
560 SEM images of vertical cross sections of the bacterial IM (A) and mammalian comparator  
561 model (B) without underlying Transwell<sup>®</sup> filter, indicating similarity in model thickness  
562 (Images are representative of n=3 investigations, with mean values of  $156 \pm 18 \mu\text{m}$  and  $165 \pm$   
563  $6 \mu\text{m}$  for the IM and mammalian comparator model respectively).

564

565

566 3.2 Evaluating the impact of model lipid composition on the permeability behavior of  
567 compounds/drugs

568 The characterization measures employed in previous sections confirmed the suitability and  
569 robustness of the bacterial IM model for transport studies, as well as the mammalian model as  
570 a relevant comparator. Bacterial IM and mammalian comparator models prepared using the  
571 same standardized procedure showed a required similarity in properties such as thickness, yet  
572 demonstrated some degree of variation on both the molecular and microscale, as a function of  
573 the different employed PLs. Whether such PL-dependent variations translated into differences  
574 in permeability behavior in the IM and the mammalian comparator model was then further  
575 investigated, to discern the importance and necessity of producing a bacterial IM model  
576 specifically employing bacterial lipids in a physiologically relevant ratio.

577  
578 A set of readily-quantifiable fluorescent dyes exhibiting a range of distribution coefficients at  
579 pH 7.4 ( $\log D_{(pH\ 7.4)}$ ) was utilized in a first step in order to conduct a preliminary proof of  
580 concept study (see Supplementary Material Table S1). Point-wise differences in  $P_{app}$  values of  
581 such compounds in the IM and the mammalian comparator were noted, showing a trend for  
582 greater compound permeation across the IM model (Fig. 6A). This was seen to occur even in  
583 case of the negatively charged dyes calcein and fluorescein, which could potentially have  
584 been predicted to interact with negatively charged PLs (such as POPG and CL of the IM) in a  
585 repulsive way, resulting in a low level of permeation [33]. Following this encouraging  
586 preliminary result, it was decided to test a set of compounds which also varied in lipophilicity,  
587 but which showed a much greater similarity with respect to other physicochemical parameters  
588 (Table 2). For this purpose  $\beta$ -blockers were selected, as a standard compound set frequently  
589 employed in cell- [34] and lipid-based [35,36] *in vitro* models for determination of  
590 discriminatory capabilities. Utilizing this set of compounds additionally allowed for  
591 permeability comparisons of the original PC-containing PVPA model with the current



592 mammalian comparator, further confirming its appropriateness to serve as a reference model  
593 in the current work (see Supplementary Material Figure S5).

594

595 **Table 2.** Important physicochemical parameters of employed  $\beta$ -blockers.

$\beta$ -blocker	$\log D_{(\text{pH } 7.4)}^{\text{a)}$	$M_w$ (g/mol)	PSA ( $\text{\AA}^2$ ) <sup>b)</sup>	H-bond donors/acceptors <sup>b)</sup>
Atenolol	-1.29	266.3	94.6	3 / 4
Metoprolol	-0.16	267.4	58.4	2 / 4
Timolol	0.03	316.4	85.2	2 / 8
Nadolol	0.68	309.4	88.8	4 / 5
Acebutolol	0.83	336.4	92.8	3 / 5
Alprenolol	1.38	249.3	43.7	2 / 3

596

PSA: polar surface Area

597

<sup>a)</sup> Values from Zhu *et al.*[37])

598

<sup>b)</sup> Values from Pubchem

599

600 Pair-wise comparisons of  $\beta$ -blocker permeability data again revealed significant point-wise  
601 differences in  $P_{\text{app}}$  values (Fig. 6B), with a higher degree of permeation noted in the case of  
602 the IM model in contrast to the mammalian comparator across the entire tested range of  
603 compound lipophilicities. This observation further confirms the impact of model lipid  
604 composition on compound permeability behavior.

605

606

607

608

609

610

611  
612  
613  
614  
615  
616  
617  
618  
619  
620  
621  
622  
623  
624  
625  
626  
627  
628  
629  
630  
631  
632  
633  
634  
635

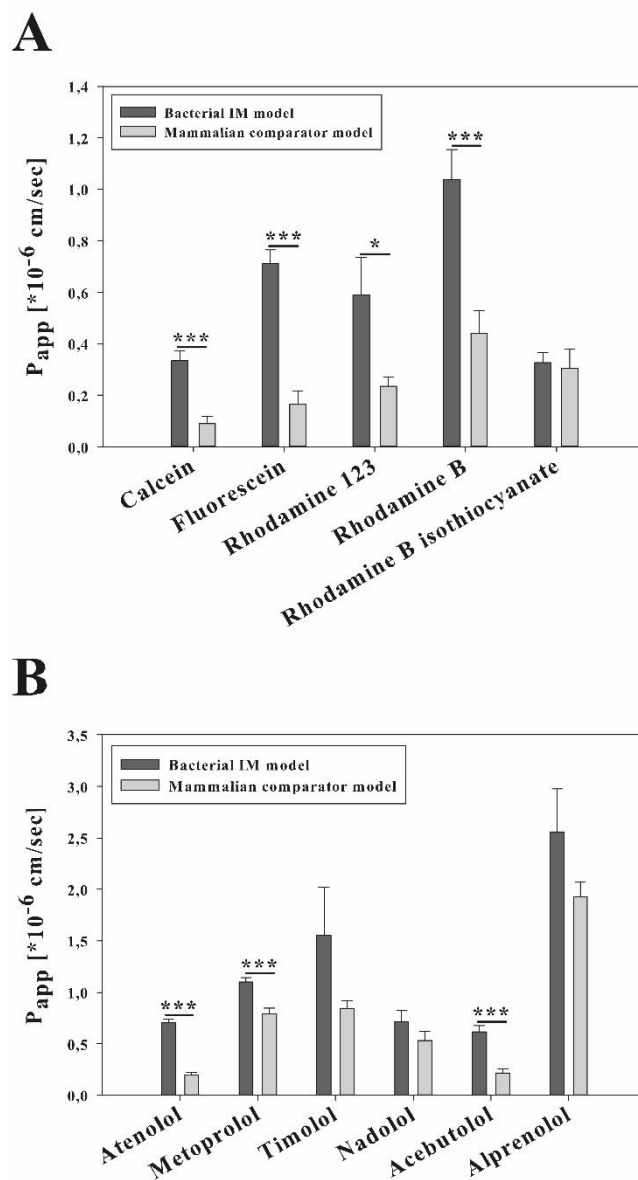


**Fig. 6.** Permeability experiment results of model compounds.  $P_{app}$  values of fluorescent dyes (A) and  $\beta$ -blockers (B), both in order of increasing lipophilicity, in the bacterial IM and mammalian comparator model. Values represent mean  $\pm$  SE;  $n \geq 9$  from 3 individual experiments; \*= $P < 0.05$ , \*\*\*= $P < 0.001$ .

636 3.3 Permeation and interaction of anti-infectives with the IM model in comparison to the  
637 mammalian comparator model

638 The assessment and comparison of model compound permeability in the IM and mammalian  
639 comparator model demonstrated an impact of the PL composition on compound permeation.  
640 It was then further investigated whether this also applies in the case of anti-infective  
641 compounds. Ciprofloxacin and minocycline, antibiotics from two different classes which need  
642 to cross the IM to reach their target [38], were therefore tested and compared in both models.  
643 The results again revealed significant differences in  $P_{app}$  values, with both antibiotics  
644 permeating across the IM model to a greater extent than the mammalian comparator (Fig.  
645 7A). The employment of bacteria-specific lipids in a permeation model of the IM (as well as  
646 in further bacterial envelope model development) is therefore deemed to be of great  
647 importance, in order to avoid underestimation of compound permeability - a problem which  
648 could be even further exacerbated when additional permeation barriers of the bacterial cell  
649 envelope (such as the OM) are taken into account.

650  
651 In a further step, an additional antibiotic, PMB, was employed in conjunction with either  
652 ciprofloxacin or minocycline, in order to investigate the existence of functional similarity  
653 between the bacterial IM model and the Gram-negative bacterial inner membrane itself. PMB  
654 is known to interact in an electrostatic manner at *in cellulo* assay concentrations [39] with  
655 acidic PLs such as POPG and CL, as found in the Gram-negative bacterial inner membrane  
656 [40,41]; this interaction is followed by insertion into the membrane structure, pore formation  
657 and subsequent weakening of the membrane barrier function. In contrast, at similar PMB  
658 concentrations, no such interaction and disruption is observed with membranes containing  
659 overall electroneutral PLs like PC [40], as present in the mammalian comparator model. As a  
660 result of its permeabilizing effect on the Gram-negative inner membrane, PMB may be used  
661 clinically in a combination therapy approach together with other antibiotics such as the

662 currently employed minocycline [42,43], in order to provide enhanced cytoplasmic entry and  
663 target access. To determine whether this scenario was reflected in the current *in vitro*  
664 approach, both models were incubated with PMB in a relevant *in cellulo* assay concentration,  
665 as previously shown to affect the IM of *Escherichia coli* [40]. Ciprofloxacin or minocycline  
666 were then applied to the models, and compound permeation was again assessed. Both  
667 ciprofloxacin and minocycline showed significantly higher  $P_{app}$  values in the IM model  
668 following PMB treatment (Fig. 7B), whereas no significant difference in  $P_{app}$  was noted for  
669 either antibiotic in the mammalian comparator model as a result of incubation with PMB (Fig.  
670 7B). The observed permeabilization of the IM model (and corresponding lack of effect in the  
671 mammalian comparator model) confirms a functional similarity of this structure to the Gram-  
672 negative bacterial inner membrane. This study therefore provides a clear example of the  
673 superior capacity of the bacterial IM model for evaluation of anti-infective permeation, further  
674 highlighting the importance of employing bacteria-specific lipids in model development.

675

676

677

678

679

680

681

682

683

684

685

686

687  
688  
689  
690  
691  
692  
693  
694  
695  
696  
697  
698  
699  
700  
701  
702  
703  
704  
705  
706  
707  
708

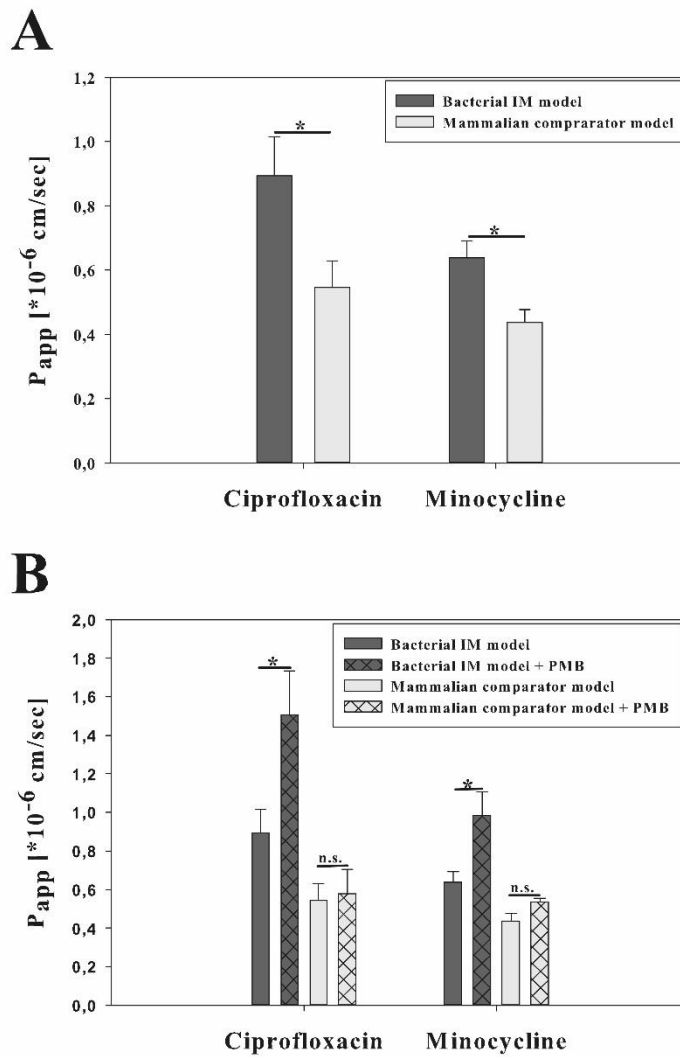


**Fig. 7.** Permeability experiment results of anti-infectives.  $P_{app}$  values of ciprofloxacin and minocycline in the bacterial IM and mammalian comparator model are shown (A), and are compared with  $P_{app}$  values following pre-incubation of both models with PMB (B). Values represent mean  $\pm$  SE;  $n=6$  from 2 individual experiments;  $*=P<0.05$ , n.s. = not significant.

709 3.4 Comparison of the IM model to an established vesicle-based assay

710 Following clear demonstration of the advantage and need for the bacterial IM model, the IM  
711 model permeation of an anti-infective-derived structure was investigated in a final, small scale  
712 exploratory study, to allow for clear comparison of data obtained with the current model to  
713 that derived from an established anti-infective permeation assay. In this respect, a  
714 hydroxyguanidine-functionalized fatty acid moiety derived from the muraymycin A-series of  
715 nucleoside antibiotics was chosen – this structure is proposed to account for the increased  
716 activity of the A-series congeners in comparison to other muraymycins, due to its ability to  
717 facilitate an increase in membrane permeability [44,45]. Recently, a simplified model system  
718 was employed to experimentally validate this proposed. In this respect, the hydroxyguanidine-  
719 functionalized fatty acid moiety, covalently linked to a fluorophore (AlexaFluor 488), was  
720 applied in a vesicle-based *in vitro* model (not entirely utilizing bacteria-relevant PL  
721 components) [23]. For comparison, a reference compound, lacking the hydroxyguanidine-  
722 functionalized fatty acid motif, was employed. The functionalized fatty acid was observed to  
723 permeate into lipid vesicles to a greater extent than the reference compound, assessed by  
724 evaluating the fluorescence intensity inside vesicles relative to background; furthermore, the  
725 functionalized fatty acid was seen to accumulate at the membrane interface right after the  
726 addition of the compound to the immobilized vesicles [23]. However, it could not be  
727 elucidated if this accumulation corresponded to a rapid permeation of the compound, due to  
728 insufficient assay sensitivity.

729

730 In the current work, as for the previous vesicle-based study, the permeability of the  $\omega$ -  
731 hydroxyguanidinylated fatty acid conjugate was assessed in comparison to the reference  
732 compound composed of the fluorescent label and linker alone (see Supplementary Material  
733 Figure S6). Higher permeation rates as well as a significantly higher  $P_{app}$  value were found for  
734 the functionalized fatty acid as compared to the reference compound in the bacterial IM

735 model (Fig. 8), confirming the previous findings of the vesicle-based assay [23]. A further  
736 very notable result from the kinetically-resolved data as shown in Fig. 8A is the high  
737 permeated amount of the functionalized fatty acid conjugate at 0 h. This observation strongly  
738 suggests that the previously noted rapid accumulation effect does seem to correlate with  
739 immediate membrane permeation, followed by a second permeation phase. This two-phase  
740 model for the permeation of the functionalized fatty acid conjugate could only be derived  
741 from kinetically-resolved data as facilitated by use of the IM model, thus further highlighting  
742 the relevance of this new approach.

743

744

745

746

747

748

749

750

751

752

753

754

755

756

757

758

759  
760  
761  
762  
763  
764  
765  
766  
767  
768  
769  
770  
771  
772  
773  
774  
775  
776  
777  
778  
779  
780  
781  
782  
783  
784

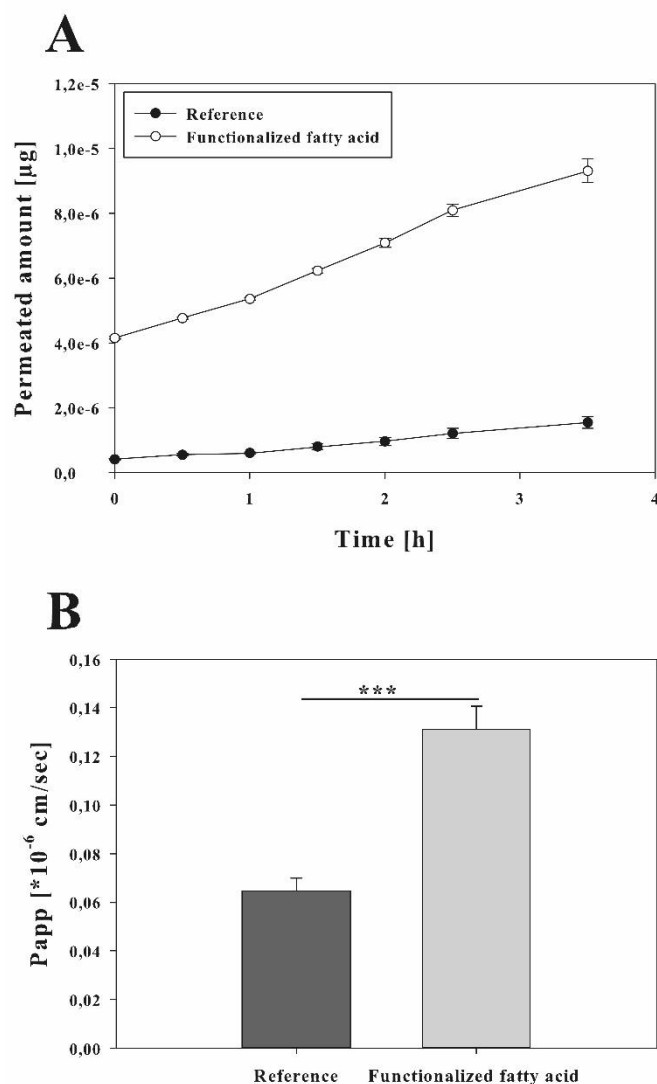


**Fig. 8.** Permeability experiment results of employed functionalized fatty acid moieties. Permeation rate and extent of the hydroxyguanidinylated fatty acid and reference compound (A), showing a permeability enhancing effect of the functionalized fatty acid moiety. The finding is also reflected in the calculated  $P_{app}$  values (B), additionally highlighting the advantage of the IM model for quantification of permeation processes and assessment of the permeation kinetics of tested compounds. Values represent mean  $\pm$  SE;  $n=9$  from 3 individual experiments;  $***=P<0.001$ .



#### 785 **4. Conclusion**

786 We herein report the successful development of a stable and robust *in vitro* permeation model  
787 of the Gram-negative bacterial IM, composed of bacteria-relevant PLs in a physiological  
788 ratio. Characterization of the IM model and its components from the molecular level to the  
789 macroscale, and comparison with an identically-produced model created from mammal-  
790 relevant PC indicated a number of PL-related model deviations. These deviations were  
791 ultimately shown to translate to significant differences in permeability of both model  
792 compounds as well as anti-infectives as a function of model PL composition. The ability of  
793 the novel IM model setup to provide quantitative data regarding the rate and extent of  
794 compound permeation was also demonstrated, facilitating a more accurate characterization of  
795 compound permeation as well as more information-rich evaluation of drug delivery  
796 approaches across the IM models. Future work focuses on the development of an OM model,  
797 in a further step towards creating a relevant permeation model of the complete Gram-negative  
798 bacterial cell envelope.

799

#### 800 **Acknowledgements**

801 The authors acknowledge Christoph Pauly (Department of Material Science And Engineering,  
802 Chair of Functional Materials, Saarland University) for his assistance in the laser scanning  
803 interferometry analysis, and the Core Facility for Integrated Microscopy, Faculty of Health  
804 and Medical Sciences, University of Copenhagen for the assistance in taking the cryo-SEM  
805 images.

806

#### 807 **Funding**

808 This research did not receive any specific grant from funding agencies in the public,  
809 commercial, or not-for-profit sectors.

810

811 **References**

- 812 [1] E.M. Wellington, A.B. Boxall, P. Cross, E.J. Feil, W.H. Gaze, P.M. Hawkey, A.S.  
813 Johnson-Rollings, D.L. Jones, N.M. Lee, W. Otten, C.M. Thomas, A.P. Williams, The role of  
814 the natural environment in the emergence of antibiotic resistance in gram-negative bacteria,  
815 *Lancet Infect. Dis.*, 13 (2013) 155-165.
- 816 [2] M. McKenna, Antibiotic resistance: the last resort, *Nature*, 499 (2013) 394-396.
- 817 [3] F.C. Tenover, Mechanisms of antimicrobial resistance in bacteria, *Am. J. Med.*, 119  
818 (2006) 3-10.
- 819 [4] M. Thein, G. Sauer, N. Paramasivam, I. Grin, D. Linke, Efficient subfractionation of  
820 gram-negative bacteria for proteomics studies, *J. Proteome Res.*, 9 (2010) 6135-6147.
- 821 [5] M.L. Nelson, Grier, M.C., Barbaro, S. E., and Ismail M. Y., Polyfunctional antibiotics  
822 affecting bacterial membrane dynamics, *Anti-Infect. Agents Med. Chem.*, 8 (2009) 3-16.
- 823 [6] H.I. Zgurskaya, C.A. López, S. Gnanakaran, Permeability barrier of Gram-negative cell  
824 envelopes and approaches to bypass it, *ACS Infect. Dis.*, 1 (2015) 512-522.
- 825 [7] T.J. Silhavy, D. Kahne, S. Walker, The bacterial cell envelope, *Cold Spring Harb.*  
826 *Perspect. Biol.*, 2 (2010) a000414.
- 827 [8] F. Graef, S. Gordon, C.M. Lehr, Anti-infectives in drug delivery-overcoming the Gram-  
828 negative bacterial cell envelope, *Curr. Top. Microbiol. Immunol.*, (2016) epub ahead of print  
829 1-22.
- 830 [9] K. Takroui, H.D. Cooper, A. Spaulding, P. Zucchi, B. Koleva, D.C. Cleary, W. Tear, P.J.  
831 Beuning, E.B. Hirsch, J.B. Aggen, Progress against *Escherichia coli* with the oxazolidinone  
832 class of antibacterials: Test case for a general approach to improving whole-cell Gram-  
833 negative activity, *ACS Infect. Dis.*, 2 (2016) 405-426.
- 834 [10] J.M. Pages, C.E. James, M. Winterhalter, The porin and the permeating antibiotic: a  
835 selective diffusion barrier in Gram-negative bacteria, *Nat. Rev. Microbiol.*, 6 (2008) 893-903.
- 836 [11] E.M. Nestorovich, C. Danelon, M. Winterhalter, S.M. Bezrukov, Designed to penetrate:  
837 time-resolved interaction of single antibiotic molecules with bacterial pores, *Proc. Natl. Acad.*  
838 *Sci. U. S. A.*, 99 (2002) 9789-9794.
- 839 [12] J. van Weerd, M. Karperien, P. Jonkheijm, Supported lipid bilayers for the generation of  
840 dynamic cell-material interfaces, *Adv. Healthcare. Mater.*, 4 (2015) 2743-2779.
- 841 [13] A.I. Kuzmenko, H. Wu, F.X. McCormack, Pulmonary collectins selectively permeabilize  
842 model bacterial membranes containing rough lipopolysaccharide, *Biochemistry*, 45 (2006)  
843 2679-2685.
- 844 [14] L.A. Clifton, S.A. Holt, A.V. Hughes, E.L. Daulton, W. Arunmanee, F. Heinrich, S.  
845 Khalid, D. Jefferies, T.R. Charlton, J.R. Webster, C.J. Kinane, J.H. Lakey, An accurate in  
846 vitro model of the *E. coli* envelope, *Angew. Chem., Int. Ed. Engl.*, 54 (2015) 11952-11955.
- 847 [15] D.I. Fernandez, A.P. Le Brun, T.H. Lee, P. Bansal, M.I. Aguilar, M. James, F. Separovic,  
848 Structural effects of the antimicrobial peptide maculatin 1.1 on supported lipid bilayers, *Eur.*  
849 *Biophys. J.*, 42 (2013) 47-59.
- 850 [16] T. Mach, P. Neves, E. Spiga, H. Weingart, M. Winterhalter, P. Ruggerone, M. Ceccarelli,  
851 P. Gameiro, Facilitated permeation of antibiotics across membrane channels-interaction of the  
852 quinolone moxifloxacin with the OmpF channel, *J. Am. Chem. Soc.*, 130 (2008) 13301-  
853 13309.
- 854 [17] M. Luckey, H. Nikaido, Specificity of diffusion channels produced by lambda phage  
855 receptor protein of *Escherichia coli*, *Proc. Natl. Acad. Sci. U. S. A.*, 77 (1980) 167-171.
- 856 [18] J.L. Gornall, K.R. Mahendran, O.J. Pambos, L.J. Steinbock, O. Otto, C. Chimere, M.  
857 Winterhalter, U.F. Keyser, Simple reconstitution of protein pores in nano lipid bilayers, *Nano*  
858 *Lett.*, 11 (2011) 3334-3340.
- 859 [19] K. Lewis, Antibiotics: Recover the lost art of drug discovery, *Nature*, 485 (2012) 439-  
860 440.

861 [20] G.E. Flaten, A.B. Dhanikula, K. Luthman, M. Brandl, Drug permeability across a  
862 phospholipid vesicle based barrier: a novel approach for studying passive diffusion, *Eur. J.*  
863 *Pharm. Sci.*, 27 (2006) 80-90.

864 [21] R.M. Epan, R.F. Epan, Bacterial membrane lipids in the action of antimicrobial agents,  
865 *J. Pept. Sci.*, 17 (2011) 298-305.

866 [22] A.D. Bangham, M.M. Standish, J.C. Watkins, Diffusion of univalent ions across the  
867 lamellae of swollen phospholipids, *J. Mol. Biol.*, 13 (1965) 238-252.

868 [23] O. Ries, C. Carnarius, C. Steinem, C. Ducho, Membrane-interacting properties of the  
869 functionalised fatty acid moiety of muraymycin antibiotics, *Med. Chem. Comm.*, 6 (2015)  
870 879-886.

871 [24] J.T. Davies, E.K. Rideal, *Interfacial phenomena*, Academic Press, New York, 1963.

872 [25] D. Marsh, Lateral pressure in membranes, *Biochim. Biophys. Acta*, 1286 (1996) 183-  
873 223.

874 [26] G.E. Flaten, H. Bunjes, K. Luthman, M. Brandl, Drug permeability across a phospholipid  
875 vesicle-based barrier 2. Characterization of barrier structure, storage stability and stability  
876 towards pH changes, *Eur. J. Pharm. Sci.*, 28 (2006) 336-343.

877 [27] G.E. Flaten, M. Skar, K. Luthman, M. Brandl, Drug permeability across a phospholipid  
878 vesicle based barrier: 3. Characterization of drug-membrane interactions and the effect of  
879 agitation on the barrier integrity and on the permeability, *Eur. J. Pharm. Sci.*, 30 (2007) 324-  
880 332.

881 [28] S.M. Fischer, G.E. Flaten, E. Hagesaether, G. Fricker, M. Brandl, In-vitro permeability  
882 of poorly water soluble drugs in the phospholipid vesicle-based permeation assay: the  
883 influence of nonionic surfactants, *J. Pharm. Pharmacol.*, 63 (2011) 1022-1030.

884 [29] F. Leonard, E.M. Collnot, C.M. Lehr, A three-dimensional coculture of enterocytes,  
885 monocytes and dendritic cells to model inflamed intestinal mucosa in vitro, *Mol. Pharm.*, 7  
886 (2010) 2103-2119.

887 [30] C.I. Grainger, L.L. Greenwell, D.J. Lockley, G.P. Martin, B. Forbes, Culture of Calu-3  
888 cells at the air interface provides a representative model of the airway epithelial barrier,  
889 *Pharm. Res.*, 23 (2006) 1482-1490.

890 [31] S.P. Gantzsch, B. Kann, M. Ofer-Glaessgen, P. Loos, H. Berchtold, S. Balbach, T.  
891 Eichinger, C.M. Lehr, U.F. Schaefer, M. Windbergs, Characterization and evaluation of a  
892 modified PVPA barrier in comparison to Caco-2 cell monolayers for combined dissolution  
893 and permeation testing, *J. Control. Release*, 175 (2014) 79-86.

894 [32] A. Avdeef, *Absorption and drug development: Solubility, permeability and charge state*,  
895 Wiley, Hoboken, NJ, USA, 2012.

896 [33] A. Malkia, L. Murtomaki, A. Urtti, K. Kontturi, Drug permeation in biomembranes: in  
897 vitro and in silico prediction and influence of physicochemical properties, *Eur. J. Pharm. Sci.*,  
898 23 (2004) 13-47.

899 [34] A.M. Marino, M. Yarde, H. Patel, S. Chong, P.V. Balimane, Validation of the 96 well  
900 Caco-2 cell culture model for high throughput permeability assessment of discovery  
901 compounds, *Int. J. Pharm.*, 297 (2005) 235-241.

902 [35] M. Kansy, F. Senner, K. Gubernator, Physicochemical high throughput screening:  
903 parallel artificial membrane permeation assay in the description of passive absorption  
904 processes, *J. Med. Chem.*, 41 (1998) 1007-1010.

905 [36] A. Avdeef, The rise of PAMPA, *Expert Opin. Drug Metab. Toxicol.*, 1 (2005) 325-342.

906 [37] C. Zhu, L. Jiang, T.M. Chen, K.K. Hwang, A comparative study of artificial membrane  
907 permeability assay for high throughput profiling of drug absorption potential, *Eur. J. Med.*  
908 *Chem.*, 37 (2002) 399-407.

909 [38] R.E.W. Hancock, A. Bell, Antibiotic uptake into Gram-negative bacteria, in: G.G.  
910 Jackson, H.D. Schlumberger, H.J. Zeiler (Eds.), *Perspectives in anti-infective therapy*,  
911 Wiesbaden 1989, pp 11-29.

912 [39] R. Daugelavicius, E. Bakiene, D.H. Bamford, Stages of polymyxin B interaction with the  
913 Escherichia coli cell envelope, *Antimicrob. Agents Chemother.*, 44 (2000) 2969-2978.  
914 [40] D.R. Storm, K.S. Rosenthal, P.E. Swanson, Polymyxin and related peptide antibiotics,  
915 *Annu. Rev. Biochem.*, 46 (1977) 723-763.  
916 [41] M. Teuber, J. Bader, Action of polymyxin B on bacterial membranes. Binding capacities  
917 for polymyxin B of inner and outer membranes isolated from Salmonella typhimurium G30,  
918 *Arch. Microbiol.*, 109 (1976) 51-58.  
919 [42] Y. Zhang, F. Chen, E. Sun, R. Ma, C. Qu, L. Ma, In vitro antibacterial activity of  
920 combinations of fosfomycin, minocycline and polymyxin B on pan-drug-resistant  
921 Acinetobacter baumannii, *Exp. Ther. Med.*, 5 (2013) 1737-1739.  
922 [43] D.R. Bowers, H. Cao, J. Zhou, K.R. Ledesma, D. Sun, O. Lomovskaya, V.H. Tam,  
923 Assessment of minocycline and polymyxin B combination against Acinetobacter baumannii,  
924 *Antimicrob. Agents. Chemother.*, 59 (2015) 2720-2725.  
925 [44] L.A. McDonald, L.R. Barbieri, G.T. Carter, E. Lenoy, J. Lotvin, P.J. Petersen, M.M.  
926 Siegel, G. Singh, R.T. Williamson, Structures of the muraymycins, novel peptidoglycan  
927 biosynthesis inhibitors, *J. Am. Chem. Soc.*, 124 (2002) 10260-10261.  
928 [45] D. Wiegmann, S. Koppermann, M. Wirth, G. Niro, K. Leyrer, C. Ducho, Muraymycin  
929 nucleoside-peptide antibiotics: uridine-derived natural products as lead structures for the  
930 development of novel antibacterial agents, *Beilstein J. Org. Chem.*, 12 (2016) 769-795.  
931  
932  
933  
934